

Modelling and Analysis of Tendon-Driven Parallel Continuum Robots under Constant Curvature and Pseudo-Rigid-Body Assumptions

Kefei Wen

Continuum Robotics Laboratory,
Department of Mathematical & Computational Sciences,
University of Toronto,
Mississauga, ON L5L 1C6, Canada
Email: kefei.wen@utoronto.ca

Jessica Burgner-Kahrs*

Continuum Robotics Laboratory,
Department of Mathematical & Computational Sciences,
University of Toronto,
Mississauga, ON L5L 1C6, Canada
Email: jessica.burgnerkahrs@utoronto.ca

This paper unifies the approaches of kinematic and static modelling, and singularity analysis for tendon-driven parallel continuum robots under constant curvature as well as pseudo-rigid-body assumptions with those implemented in conventional rigid parallel robots. Constraint conditions are determined for the legs of this type of parallel continuum robots, based on which the velocity equations and Jacobian matrices are derived. These are further exploited for inverse kinematic and singularity analysis. Static models for the robot as well as for each of the continuum links under pseudo-rigid-body assumption are derived. Finally, a simulation example is given to validate the kinematic models. It is shown that singularities can be determined using Grassmann line geometry or by detecting the numerical values of three performance indices.

1 Introduction

A continuum robot is defined as an actuatable structure whose constitutive material forms curves with continuous tangent vectors [1]. The very nature of inherent compliance and ease of miniaturization make them suitable for interventional medicine and surgery [1–3], in-situ maintenance, repair and operations [4], and space explorations [5]. Modelling of continuum robots is performed using diverse approaches such as: constant curvature (CC) assumption [6–8], Cosserat rod theory [9–12], and pseudo-rigid-body (PRB) assumption [13–17]. A more comprehensive review on the applications and modelling methods of continuum robots can

be found in [1, 18] and the references therein.

Recently, combinations of continuum/soft robots with parallel structures are emerging as parallel continuum/soft robots. Such robots can benefit from the advantages of parallel robots, e.g., high stiffness and high operation speed, when compared to continuum robots. Meanwhile, the characteristic of light weight allows them to be favourable interfaces for safe physical human-robot interaction. In the last few years, several parallel continuum/soft robots were proposed (see, for instance [19–29]), in which the motion of the continuum segments is realized through diverse actuation paradigms.

In the architectures proposed in [19] and [22], linear and rotary actuators are attached to the proximal end of a continuum rod to change its length between the moving platform and base of a 6-degrees-of-freedom (6-DOF) Stewart platform [19] and to produce a deformation of the rod of a planar 2-DOF parallel continuum manipulator [22], respectively. In addition to the use of continuum segments as the links, they are designed as continuum joints to replace the conventional rigid joints of a parallel robot. One of such continuum joints is developed in [24], in which each backbone can bend passively while sliding in the holes of spacer disks by exerting an external wrench to the distal end or by driving the translational actuators on the base of the robot. An alternative actuation scheme consists in actively bending the continuum segments can be seen in [20] and [28], in which pneumatic and tendon actuations are respectively utilised to inflate the chambers of the soft parallel robots [20] and to drive the continuum links of the parallel continuum robots (PCRs) [28]. Cosserat rod theory [19] and its special case Kirchhoff rod theory [22, 26], as well as CC assumption [28]

*Corresponding author.

are implemented in the modelling of these robots. More recently proposed parallel continuum/soft robots are enumerated and discussed in [28].

In this paper, we focus on the forward and differential inverse kinematic modelling, static modelling, and singularity analysis of non-redundant and kinematically redundant tendon-driven parallel continuum robots (TDPCRs) under CC and PRB assumptions. The moving platform of a common rigid parallel robot is connected to the base through several legs where each of the legs consists of rigid links and joints (see Fig. 1a). As it is illustrated in Fig. 1b, the general structure of the TDPCRs considered in this study consists of a moving platform (which is rigid) connected to the base by several identical legs, where each leg contains an actuated continuum link which is driven by two opposite tendons. Adjacent links are connected by conventional rigid joints and the existence of rigid links in some architectures is not necessary. Although Fig. 1b depicts a general spatial TDPCR, these structural features are identical to those of the planar and redundant architectures.

We build on our previous work [28], where explicit Jacobian matrices of two planar TDPCRs are provided, and singularities are detected by calculating the determinants of the Jacobian matrices, this is applied to the singularity distribution analysis within the workspace. Note, that singular configurations are not intuitively identified by an observation of the Jacobian matrices. Moreover, in [28], general structural features of a wide range of TDPCRs are not provided, and kinematic modelling is performed only based on the CC assumption, which is not directly applicable to static modelling. These limitations motivated our current study.

In the following sections, we show that under CC and PRB assumptions, the kinematic and static modelling, and singularity analysis, of TDPCRs can be conducted using the fundamental techniques which are widely implemented in modelling and control of rigid parallel robots. We seek in unifying the modelling and analysis approaches for both rigid parallel robots and TDPCRs. As one of the benefits, Jacobian matrices of the TDPCRs can be expressed in a more compact form, allowing the use of Grassmann line geometry for intuitive singularity analysis. Compared to Cosserat rod theory, one of the main advantages of the approaches provided in this study is that they are computationally efficient and the analysis is straightforward, thereby simplifying the control of the TDPCRs.

The proposed modelling and analysis approaches, which can be applied to the TDPCRs depicted in Fig. 1b, are demonstrated by several case studies. In Section 2, kinematic modelling of two planar architectures is provided. Static modelling of TDPCRs under PRB assumption is derived in Section 3. Section 4 addresses the kinematic modelling of spatial and kinematically redundant TDPCRs. Singularity analysis and an example study are presented in Section 5 to validate the kinematic models. Finally, conclusions are drawn in Section 6.

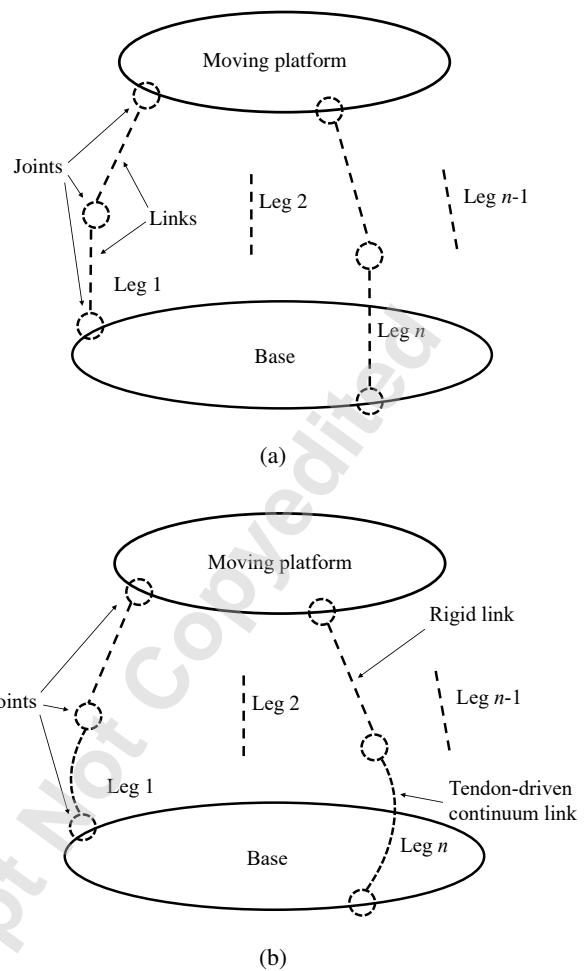


Fig. 1: Schematic representations of a common rigid parallel robot (a) and a common TDPCR (b). For simplicity, tendons of the continuum links are not shown in (b).

2 Kinematic Modelling of Planar TDPCRs

In this section, we derive the velocity equations for a TDPCR under both CC and PRB assumptions by establishing the constraint equations and demonstrate the use in two case studies for planar architectures. We then build on the velocity equations to establish the differential inverse kinematics as well as the forward kinematics of the TDPCRs. The velocity equations are also fundamental for static modelling and singularity and performance analysis, as will be shown in the following sections.

2.1 Constant Curvature Assumption

In this subsection, we look at the kinematics of planar 3-RFR and 3-FRR TDPCRs under the CC assumption. Note, that we use \bar{R} to denote a passive revolute joint and \bar{F} for an actuated continuum link.

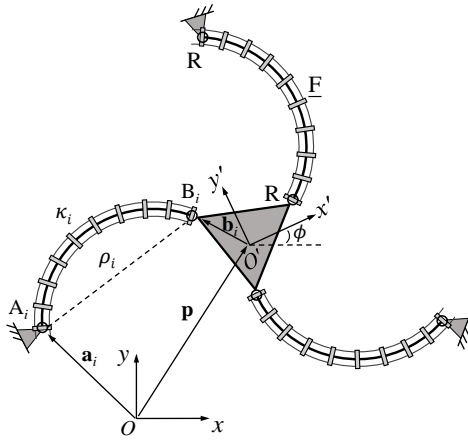


Fig. 2: Geometric description of a planar three-DOF 3-RFR TDPCR.

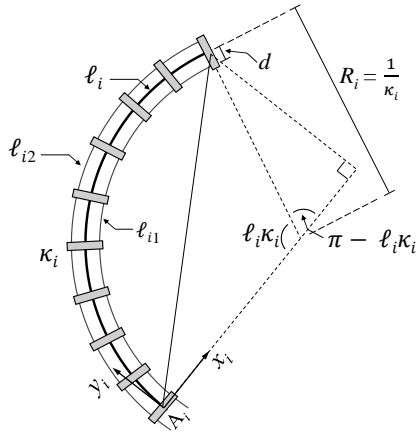


Fig. 3: Geometric parameters of one of the continuum links.

2.1.1 3-RFR TDPCR

The planar 3-RFR TDPCR consists of a rigid moving platform connected to the base by three identical RFR legs (see Fig. 2). Each of the continuum links is actuated by two tendons which are deployed on both sides of the backbone and pass through a number of spacer disks. Thus, the continuum link can produce an in-plane (coplanar with the base and moving platform) bending of its backbone (see, for instance [28]). Points A_i and B_i (with $i = 1, 2, 3$) are the centres of the revolute joints on the base and moving platform in the i -th leg, respectively. A fixed coordinate frame Oxy is defined on the base, while a moving coordinate frame $O'x'y'$ is attached to the moving platform.

Three constraint equations can be established for the TDPCR. In each leg, the squared distance between points A_i and B_i , noted ρ_i^2 , is written as

$$\rho_i^2 = (\mathbf{p} + \mathbf{Q}\mathbf{b}_{i0} - \mathbf{a}_i)^T (\mathbf{p} + \mathbf{Q}\mathbf{b}_{i0} - \mathbf{a}_i), \quad i = 1, 2, 3 \quad (1)$$

where $\mathbf{p} \in \mathbb{R}^2$ and $\mathbf{Q} \in SO(2)$ are the position vector and rotation matrix of the moving platform with respect to the base frame, \mathbf{a}_i is the position vector of point A_i , \mathbf{b}_{i0} is the (constant) position vector of point B_i , directed from point O' to point B_i and is expressed in the moving frame. This vector is noted \mathbf{b}_i when expressed in the base frame. The rotation matrix \mathbf{Q} is expressed as

$$\mathbf{Q} = \begin{bmatrix} \cos \phi & -\sin \phi \\ \sin \phi & \cos \phi \end{bmatrix} \quad (2)$$

where ϕ is the angle between the x' -axis of the moving frame and the x -axis of the base frame.

The time derivative of Eq. (1) yields

$$\rho_i \dot{\rho}_i = \mathbf{r}_i^T \dot{\mathbf{p}} + \dot{\phi} \mathbf{r}_i^T \mathbf{E} \mathbf{Q} \mathbf{b}_{i0}, \quad i = 1, 2, 3 \quad (3)$$

where

$$\mathbf{r}_i = \mathbf{p} + \mathbf{Q}\mathbf{b}_{i0} - \mathbf{a}_i, \quad (4)$$

$\dot{\phi}$ is the angular velocity of the moving platform, and

$$\dot{\phi} \mathbf{E} \mathbf{Q} = \dot{\mathbf{Q}} \quad (5)$$

with

$$\mathbf{E} = \begin{bmatrix} 0 & -1 \\ 1 & 0 \end{bmatrix}. \quad (6)$$

Since ρ_i can be expressed in terms of the curvature (κ_i) and length (ℓ_i) of the backbone of the i -th continuum link, i.e.,

$$\rho_i = \frac{2}{\kappa_i} \sin\left(\frac{\ell_i \kappa_i}{2}\right), \quad i = 1, 2, 3, \quad (7)$$

one can then obtain

$$\dot{\rho}_i = \alpha_i \dot{\kappa}_i \quad (8)$$

with

$$\alpha_i = \frac{\ell_i}{\kappa_i} \cos\left(\frac{\ell_i \kappa_i}{2}\right) - \frac{\rho_i}{\kappa_i}. \quad (9)$$

The curvature of the i -th continuum link is generated by controlling the lengths of the corresponding tendons. Thus, it is reasonable to express κ_i in terms of the time derivative of the lengths of the tendons in the same leg. As it can be observed from Fig. 3, the central angle, $\ell_i \kappa_i$, is expressed as

$$\ell_i \kappa_i = \frac{\ell_{i1}}{R_i - d} = \frac{\ell_{i2}}{R_i + d} \quad (10)$$

where d is the distance between the backbone and each of the tendons, and ℓ_{ij} (with $j = 1, 2$) is the length of the j -th tendon in the i -th continuum link. The relationship between the (non-negative) curvature and the tendons' lengths in the i -th continuum link is then determined by replacing R_i with $\frac{1}{\kappa_i}$ (see Fig. 3) and eliminating the term $\ell_i \kappa_i$, which is expressed as

$$\kappa_i = \left| \frac{\ell_{i2} - \ell_{i1}}{d(\ell_{i1} + \ell_{i2})} \right|, \quad i = 1, 2, 3. \quad (11)$$

Taking the time derivative of κ_i leads to

$$\dot{\kappa}_i = \frac{h}{\kappa_i} \frac{2(\ell_{i1}\dot{\ell}_{i2} - \ell_{i2}\dot{\ell}_{i1})}{d(\ell_{i1} + \ell_{i2})^2} \quad (12)$$

with

$$h = \frac{\ell_{i2} - \ell_{i1}}{d(\ell_{i1} + \ell_{i2})}, \quad (13)$$

and where the elongation of the tendon is not considered. Since $\dot{\ell}_{i2} = -\dot{\ell}_{i1}$, i.e. both tendons have to be changed by the same amount in opposing directions, $\dot{\kappa}_i$ can then be rewritten in the following form by replacing $\dot{\ell}_{i2}$ with $-\dot{\ell}_{i1}$ in Eq. (12)

$$\dot{\kappa}_i = \lambda_i \dot{\ell}_{i1} \quad (14)$$

with

$$\lambda_i = -\frac{h}{\kappa_i} \frac{2}{d(\ell_{i1} + \ell_{i2})}, \quad i = 1, 2, 3, \quad (15)$$

and where the value of $\frac{h}{\kappa_i}$ is determined by

$$\frac{h}{\kappa_i} = \begin{cases} 1 & \text{if } \ell_{i1} < \ell_{i2} \\ -1 & \text{if } \ell_{i1} > \ell_{i2} \\ \text{Undefined} & \text{otherwise.} \end{cases} \quad (16)$$

Substituting Eq. (14) into Eq. (8), and then substituting Eq. (8) into Eq. (3) and rearranging the terms, one can obtain

$$\mathbf{J}\mathbf{t} = \mathbf{K}\dot{\boldsymbol{\ell}} \quad (17)$$

which are the velocity equations of the 3-RFR TDPCR and where \mathbf{J} and \mathbf{K} are the Jacobian matrices, $\mathbf{t} = [\dot{\mathbf{p}}^T \dot{\phi}]^T$ is the vector of the Cartesian velocities, and $\dot{\boldsymbol{\ell}}$ is the vector of the time derivative of the lengths of the tendons, namely $\dot{\boldsymbol{\ell}} = [\dot{\ell}_{11} \dot{\ell}_{21} \dot{\ell}_{31}]^T$. The Jacobian matrices are written as

$$\mathbf{J} = \begin{bmatrix} \mathbf{r}_1^T & \mathbf{r}_1^T \mathbf{E} \mathbf{Q} \mathbf{b}_{10} \\ \mathbf{r}_2^T & \mathbf{r}_2^T \mathbf{E} \mathbf{Q} \mathbf{b}_{20} \\ \mathbf{r}_3^T & \mathbf{r}_3^T \mathbf{E} \mathbf{Q} \mathbf{b}_{30} \end{bmatrix}, \quad (18)$$

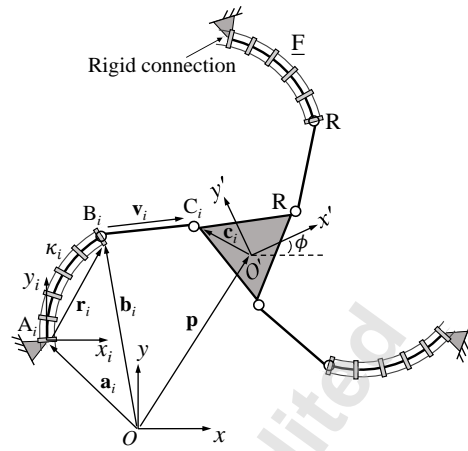


Fig. 4: Geometric description of a planar three-DOF 3-FRR TDPCR.

which is of dimension 3×3 and in which each row represents a Plücker line (similar to that of the rigid planar 3-RRR parallel manipulator) passing through points A_i and B_i , and

$$\mathbf{K} = \begin{bmatrix} k_1 & 0 & 0 \\ 0 & k_2 & 0 \\ 0 & 0 & k_3 \end{bmatrix} \quad (19)$$

which is also of dimension 3×3 and in which

$$k_i = \rho_i \alpha_i \lambda_i, \quad i = 1, 2, 3. \quad (20)$$

2.1.2 3-FRR TDPCR

The planar 3-FRR TDPCR is schematically represented in Fig. 4. The constraint equation on the constant squared length of the rigid link $B_i C_i$ in the i -th leg can be written in a form similar to that of Eq. (1), leading to

$$v_i^2 = (\mathbf{p} + \mathbf{Q}\mathbf{c}_{i0} - \mathbf{b}_i)^T (\mathbf{p} + \mathbf{Q}\mathbf{c}_{i0} - \mathbf{b}_i), \quad i = 1, 2, 3 \quad (21)$$

where $\mathbf{p} \in \mathbb{R}^2$ and $\mathbf{Q} \in SO(2)$ are the position vector of point O' and orientation matrix of the moving frame respectively, $\mathbf{Q}\mathbf{c}_{i0} = \mathbf{c}_i$ is the position vector of point C_i connecting point O' and point C_i and is denoted \mathbf{c}_{i0} when expressed in the moving frame, \mathbf{b}_i is the position vector of point B_i , and v_i is the norm of vector \mathbf{v}_i directing from point B_i to point C_i .

Differentiating Eq. (21) with respect to time yields

$$\mathbf{v}_i^T \dot{\mathbf{p}} + \dot{\phi} \mathbf{v}_i^T \mathbf{E} \mathbf{Q} \mathbf{c}_{i0} = \mathbf{v}_i^T \dot{\mathbf{b}}_i, \quad i = 1, 2, 3 \quad (22)$$

where

$$\mathbf{v}_i = \mathbf{p} + \mathbf{Q}\mathbf{c}_{i0} - \mathbf{b}_i \quad (23)$$

and matrix \mathbf{E} is defined in Eq. (6). Since $\mathbf{b}_i = \mathbf{a}_i + \mathbf{r}_i$, where \mathbf{a}_i and \mathbf{r}_i are the position vector of point A_i and the vector

connecting point A_i to point B_i respectively, and \mathbf{a}_i is a constant vector, we have $\dot{\mathbf{b}}_i = \dot{\mathbf{r}}_i$. Define

$$\mathbf{r}_i = \mathbf{Q}_i \mathbf{u}_i, \quad (24)$$

where \mathbf{Q}_i is the (constant) orientation matrix of the fixed local frame $A_i x_i y_i$ (see Figs. 3 and 4) with respect to the base frame, whose x_i -axis is along the base of the continuum link, and \mathbf{u}_i is the vector \mathbf{r}_i expressed in the corresponding local frame. As it can be observed from Fig. 3, that vector \mathbf{u}_i is expressed as

$$\mathbf{u}_i = \frac{1}{\kappa_i} \begin{bmatrix} 1 - \cos(\ell_i \kappa_i) \\ \sin(\ell_i \kappa_i) \end{bmatrix}, \quad i = 1, 2, 3 \quad (25)$$

where the definitions of ℓ_i and κ_i are similar to those given in Eq. (7). The time derivative of Eq. (25) yields

$$\dot{\mathbf{u}}_i = \mathbf{E}_i \mathbf{u}_i \dot{\kappa}_i \quad (26)$$

with

$$\mathbf{E}_i = \begin{bmatrix} -\frac{1}{\kappa_i} & \ell_i \\ \frac{\ell_i \cos(\ell_i \kappa_i)}{1 - \cos(\ell_i \kappa_i)} & -\frac{1}{\kappa_i} \end{bmatrix}, \quad i = 1, 2, 3. \quad (27)$$

One can then obtain

$$\dot{\mathbf{b}}_i = \mathbf{Q}_i \mathbf{E}_i \mathbf{u}_i \dot{\kappa}_i \quad (28)$$

where κ_i can be further expressed in terms of ℓ_{i1} (with $i = 1, 2, 3$) using Eq. (14).

The velocity equations are obtained by substituting Eq. (28) into Eq. (22) and rearranging the terms, leading to a form the same as that of Eq. (17), in which Jacobian \mathbf{J} is written as

$$\mathbf{J} = \begin{bmatrix} \mathbf{v}_1^T & \mathbf{v}_1^T \mathbf{E}_1 \mathbf{Q}_1 \mathbf{c}_{10} \\ \mathbf{v}_2^T & \mathbf{v}_2^T \mathbf{E}_2 \mathbf{Q}_2 \mathbf{c}_{20} \\ \mathbf{v}_3^T & \mathbf{v}_3^T \mathbf{E}_3 \mathbf{Q}_3 \mathbf{c}_{30} \end{bmatrix}, \quad (29)$$

where each row represents a Plücker line (similar to that of the rigid planar 3-RRR parallel manipulator) passing through points B_i and C_i , and the elements on the diagonal of Jacobian \mathbf{K} are

$$k_i = \lambda_i \mathbf{v}_i^T \mathbf{Q}_i \mathbf{E}_i \mathbf{u}_i, \quad i = 1, 2, 3. \quad (30)$$

2.2 Pseudo-rigid-body Assumption

Although the velocity equations developed in the preceding subsection are compact, they only describe a special case, i.e., no external loading. Another possible approach for approximately representing the shape of the continuum links

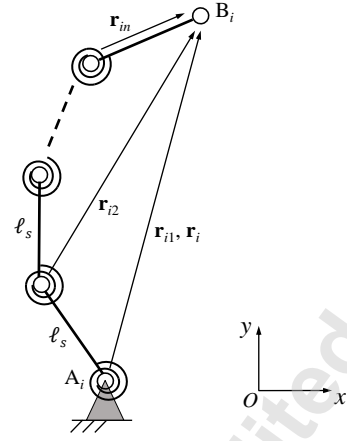


Fig. 5: Schematic representation of the PRB assumption of a continuum link of planar TDPCRs.

of a TDPCR, which can also account for external loading, is the PRB assumption [14, 16]. This approach is computationally less expensive than the Cosserat rod theory while producing comparable accuracy [16]. In addition, as will be addressed in Section 3, the PRB method allows the development of a static model for TDPCRs.

Each of the continuum links of the TDPCR is modelled as a serial linkage consisting of a number of n (with $n > 2$) rigid links with a number of n pseudo-revolute joints, in which each of them is coupled with a pseudo-torsion spring. The assumption of the pseudo-torsion spring plays an important role in calculating the joint torques, which will be discussed in detail in Section 3. The axes of the pseudo-revolute joints are orthogonal to the plane of the TDPCR. Each of the pseudo-rigid links has a constant length of ℓ_s (see Fig. 5). Under the PRB assumption, the TDPCRs can be regarded as rigid kinematically redundant parallel robots.

2.2.1 3-RFR TDPCR

The time derivative of ρ_i (with $i = 1, 2, 3$) should be determined in order to develop the velocity equations, since ρ_i cannot be expressed in a form as that shown in Eq. (7). Equation (1) can be rewritten as

$$\mathbf{r}_i^T \dot{\mathbf{r}}_i = \rho_i^2, \quad i = 1, 2, 3 \quad (31)$$

where \mathbf{r}_i is a vector directing from point A_i to point B_i , expressed in the base frame, and is defined in Eq. (4). The time derivative of Eq. (31) leads to

$$\mathbf{r}_i^T \dot{\mathbf{r}}_i = \rho_i \dot{\rho}_i \quad (32)$$

where $\dot{\mathbf{r}}_i$ is the velocity of point B_i (since \mathbf{a}_i is a constant vector) and is written as

$$\dot{\mathbf{r}}_i = \mathbf{E} [\mathbf{r}_{i1} \cdots \mathbf{r}_{in}] \begin{bmatrix} \dot{\theta}_{i1} \\ \vdots \\ \dot{\theta}_{in} \end{bmatrix} \quad (33)$$

where \mathbf{E} is defined in Eq. (6), \mathbf{r}_{ij} (with $j = 1, \dots, n$) is the vector pointing from the centre of the ij -th pseudo-revolute joint to point B_i , and $\dot{\theta}_{ij}$ is the joint velocity of the ij -th pseudo-revolute joint. The term $\mathbf{E}\mathbf{r}_{ij}$ in Eq. (33) represents the 2-dimensional cross product between the unit direction vector of the axis of ij -th pseudo-revolute joint and vector \mathbf{r}_{ij} . Substituting Eq. (33) into Eq. (32) and rearranging terms yields

$$\rho_i \dot{\rho}_i = \mathbf{r}_i^T \mathbf{E} [\mathbf{r}_{i2} \cdots \mathbf{r}_{in}] \begin{bmatrix} \dot{\theta}_{i2} \\ \vdots \\ \dot{\theta}_{in} \end{bmatrix} \quad (34)$$

where the velocity component relevant to the $i1$ -th virtual revolute joint disappears since this joint coincides with the passive revolute joint located at point A_i . Thus, we have $\mathbf{r}_{i1} = \mathbf{r}_i$ and $\mathbf{r}_i^T \mathbf{E} \mathbf{r}_{i1} = 0$. Nevertheless, the term $\dot{\theta}_{i1}$ can be included in the vector of pseudo-joint velocities by slightly shifting the proximal end of the continuum link away from the passive revolute joint on the base, which could be easily realised in a physical prototype.

The velocity equations can then be obtained by substituting Eq. (34) into Eq. (3) and rearranging the terms, leading to

$$\mathbf{J}\mathbf{t} = \mathbf{K}_\theta \dot{\boldsymbol{\theta}} \quad (35)$$

where Jacobian \mathbf{J} is identical to that given in Eq. (18), and Jacobian \mathbf{K}_θ is expressed as

$$\mathbf{K}_\theta = \begin{bmatrix} \mathbf{k}_{1\theta} & \mathbf{0} & \mathbf{0} \\ \mathbf{0} & \mathbf{k}_{2\theta} & \mathbf{0} \\ \mathbf{0} & \mathbf{0} & \mathbf{k}_{3\theta} \end{bmatrix} \quad (36)$$

which is of dimension $3 \times 3(n-1)$ with

$$\mathbf{k}_{i\theta} = \mathbf{r}_i^T \mathbf{E} [\mathbf{r}_{i2} \cdots \mathbf{r}_{in}], \quad i = 1, 2, 3 \quad (37)$$

which is of dimension $1 \times (n-1)$, where $\mathbf{0}$ is a $1 \times (n-1)$ zero vector, $\dot{\boldsymbol{\theta}}$ is a $3(n-1) \times 1$ vector of joint velocities written as $\dot{\boldsymbol{\theta}} = [\dot{\theta}_1^T \dot{\theta}_2^T \dot{\theta}_3^T]^T$ with $\dot{\theta}_i = [\dot{\theta}_{i2} \cdots \dot{\theta}_{in}]^T, i = 1, 2, 3$.

2.2.2 3-FRR TDPCR

The time derivative of vector \mathbf{r}_i (see Fig. 4), which is the velocity of point B_i , noted $\dot{\mathbf{b}}_i$ in Eq. (22), is readily determined in a form similar to that for the 3-RFR architecture

given in Eq. (33). Finally, the velocity equations are obtained by substituting $\dot{\mathbf{r}}_i$ into Eq. (22) and rearranging the terms, leading to a form similar to that given in Eq. (35), in which Jacobian \mathbf{J} is the same as that given in Eq. (29), while the components $\mathbf{k}_{i\theta}, i = 1, 2, 3$ in Jacobian \mathbf{K}_θ are written as

$$\mathbf{k}_{i\theta} = \mathbf{v}_i^T \mathbf{E} [\mathbf{r}_{i1} \cdots \mathbf{r}_{in}], \quad i = 1, 2, 3 \quad (38)$$

which is of dimension $1 \times n$. And the vector of joint velocities, $\dot{\boldsymbol{\theta}}$, in this case is of dimension $3n \times 1$, which is written as $\dot{\boldsymbol{\theta}} = [\dot{\theta}_1^T \dot{\theta}_2^T \dot{\theta}_3^T]^T$ with $\dot{\theta}_i = [\dot{\theta}_{i1} \cdots \dot{\theta}_{in}]^T, i = 1, 2, 3$.

2.3 Differential Inverse Kinematics

A feasible and straightforward way for solving the inverse kinematic problem of a TDPCR relies on the velocity equations, since an analytical solution does generally not exist. For example, assuming that matrices \mathbf{J} are of full rank, the standard forms of the velocities equations of the 3-RFR TDPCR under CC and PRB assumptions can be respectively described as the following expressions by rewriting Eqs. (17) and (35), i.e.,

$$\mathbf{t} = \mathbf{J}^{-1} \mathbf{K} \dot{\boldsymbol{\ell}} = \mathbf{U} \dot{\boldsymbol{\ell}} \quad (39)$$

and

$$\mathbf{t} = \mathbf{J}^{-1} \mathbf{K}_\theta \dot{\boldsymbol{\theta}} = \mathbf{U}_\theta \dot{\boldsymbol{\theta}}. \quad (40)$$

A unique solution of Eq. (39), which is $\dot{\boldsymbol{\ell}}$ for the CC assumption, can be obtained as

$$\dot{\boldsymbol{\ell}} = \mathbf{U}^{-1} \mathbf{t}. \quad (41)$$

Whereas a general solution of Eq. (40), which is $\dot{\boldsymbol{\theta}}$ for the PRB assumption, is obtained based on the typical technique which is used to solve the inverse kinematic problem of kinematically redundant robots [30]. The general solution consists of a minimum norm term, and an additional null space term of matrix \mathbf{U}_θ (or null space term of matrix \mathbf{K}_θ since Jacobian \mathbf{J} is of full rank) which can only produce a local motion of the legs and has no impact on the position and orientation of the moving platform of the TDPCR.

Another possibility for solving the inverse kinematic problem of PCRs is developed in [28], where a numerical root finding approach is utilised. However, the number of solutions highly depend on the initial guess, i.e., the approach may lead to multiple solutions and additional calculations are required to determine a unique solution for control purpose. Moreover, the approach is specifically developed for TDPCRs under CC assumption. Whereas, in this study, the solution determined by Eq. (41) (under CC assumption) is unique, furthermore, a general solution for TDPCRs under PRB assumption is readily obtained.

2.4 Forward Kinematics

The forward kinematic problem of TDPCRs can be solved using methods similar to those for their rigid counterparts proposed in [31–33]. For example, the solution to the forward kinematic problem of the 3-RFR TDPCR consists in calculating the Cartesian coordinates $\mathbf{p} = [x \ y]^T$ and ϕ for given actuated joint values (ρ_1, ρ_2, ρ_3) and prescribed bending direction of each of the continuum links. The equations given in Eq. (1) constitute a system of three nonlinear equations whose unknowns are x, y and ϕ . By representing $\mathbf{b}_{i0} = [B_{i0x} \ B_{i0y}]^T$ and $\mathbf{a}_i = [A_{ix} \ A_{iy}]^T$, we can rewrite Eq. (1) in the form

$$\rho_i^2 = (x + B_{i0x} \cos \phi - B_{i0y} \sin \phi - A_{ix})^2 + (y + B_{i0x} \sin \phi + B_{i0y} \cos \phi - A_{iy})^2, \quad i = 1, 2, 3. \quad (42)$$

By eliminating x and y we end up with a polynomial equation of sixth-order of T , given as

$$C_0 + C_1 T + C_2 T^2 + C_3 T^3 + C_4 T^4 + C_5 T^5 + C_6 T^6 = 0 \quad (43)$$

with $T = \tan \frac{\phi}{2}$, and the expressions of the coefficients are given in [34]. This is equivalent to solve for the forward kinematic problem of the planar 3-RPR (P stands for an actuated prismatic joint) or 3-RRR parallel manipulator, which may lead to a maximum number of six different branches.

3 Static Modelling of Planar TDPCRs: A PRB Method

Virtual work principle is applied to develop the static equations for serial and parallel robots with rigid components. However, in the presence of both rigid and continuum links, the possibility of implementation of this principle under CC assumption needs to be further investigated. Whereas virtual work principle can be applied to TDPCRs under the PRB assumption, since each of the continuum links is modelled as a pseudo-rigid serial linkage. In this section, we provide a PRB assumption based method for static modelling of the planar TDPCRs. Moreover, in addition to the static model of the entire robot, we propose a novel static model which consists of the static equations of each of the continuum links of the TDPCRs.

The main purpose of the development of the static equations is that they are useful to approximately calculate the lengths of the tendons required to drive the continuum links. Implementing the static model of a continuum link in the motion control loop will be briefly described in one of the following subsections. The verification of the accuracy of the static models for control is one of our future work and is beyond the scope of the current study. In this section, we simply provide the procedure to derive the static equations.

3.1 Static Equations for Planar TDPCRs

According to the principle of virtual work, for example, static equations of the 3-RFR TDPCR can be derived based

on Eq. (35), which are expressed as

$$\boldsymbol{\tau} = (\mathbf{J}^{-1} \mathbf{K}_\theta)^T \mathbf{F} \quad (44)$$

where $\boldsymbol{\tau} = [\boldsymbol{\tau}_1^T \ \boldsymbol{\tau}_2^T \ \boldsymbol{\tau}_3^T]^T$ (with $\boldsymbol{\tau}_i = [\tau_{i2} \ \dots \ \tau_{in}]^T, i = 1, 2, 3$) is a $3(n-1) \times 1$ vector of the virtual revolute joint torques, \mathbf{J} and \mathbf{K}_θ are the velocity Jacobians given in Eq. (35), and \mathbf{F} is a 3×1 Cartesian force and moment vector, which is also called the wrench, acting at the moving platform.

Each of the joint torques shown in Eq. (44) is related to the infinitesimal displacement of the corresponding virtual revolute joint through the torsion spring constant. This relationship is expressed as

$$\tau_{ij} = k_{ij} \delta \theta_{ij}, \quad i = 1, 2, 3 \text{ and } j = 2, \dots, n \quad (45)$$

where τ_{ij}, k_{ij} , and $\delta \theta_{ij}$ are the joint torque, the torsion spring coefficient, and the displacement of the ij -th virtual revolute joint, respectively. The spring coefficient k_{ij} is given [14, 16] by the following expression:

$$k_{ij} = \frac{EI}{\ell_s} \quad (46)$$

where E and I are respectively the Young's modulus and the area moment of inertia, and are assumed to be constant along the length of each of the continuum links.

The static equations of the 3-FRR TDPCR can be developed in a way similar to Eq. (44). However, it should be noted that, different from the physical meaning of the static equations of a rigid robot, Eq. (44) is not appropriate for detecting the magnitudes of the Cartesian wrench that can be supported by the TDPCR, because the TDPCR can only resist a relatively small external wrench due to the flexibility of the continuum links. Otherwise, a large deformation of the continuum link may be generated and the Jacobian matrices derived based on the PRB assumption will not correctly represent the real configuration of the TDPCR. A posture error threshold of the continuum link can be defined to indicate whether the Jacobian matrices in the static model are validate. For example, one can detect the difference between the real posture (measured by external or internal sensors) and the desired one and compare this difference with the threshold.

3.2 Static Modelling of Planar Continuum Links

Even if no wrench acting at the moving platform, each of the continuum links of the planar TDPCRs may still suffer from the tip force and tip moment induced by tendon tensions. In this subsection, we investigate the static modelling of the continuum links of the planar TDPCR which in turn can be exploited for motion control in the absence of Cartesian wrench.

We assume that each of the pseudo-rigid linkages of the 3-RFR TDPCR is isolated from the other parts of the robot.

Note that the tip velocity of this linkage consists of the linear velocity at end point (point B_i), which is $\dot{\mathbf{r}}_i$ given in Eq. (33), and the angular velocity at the tip, noted $\dot{\psi}_i$. The velocity equations of this linkage can be obtained by rewriting Eq. (33) into the following form

$$\dot{\mathbf{r}}_{ip} = \mathbf{J}_{ip} \dot{\boldsymbol{\theta}}_{ip}, \quad i = 1, 2, 3 \quad (47)$$

where $\dot{\mathbf{r}}_{ip} = [\dot{\mathbf{r}}_i^T \dot{\psi}_i^T]^T$ is the 3×1 vector of the linear and angular velocities at the tip,

$$\mathbf{J}_{ip} = \begin{bmatrix} \mathbf{E} [\mathbf{r}_{i1} \cdots \mathbf{r}_{in}] \\ \mathbf{1} \end{bmatrix} \quad (48)$$

which is the $3 \times n$ Jacobian of the pseudo-rigid linkage in which $\mathbf{1}$ is a $1 \times n$ vector with all elements equal to 1, and $\dot{\boldsymbol{\theta}}_{ip} = [\dot{\boldsymbol{\theta}}_{i1} \cdots \dot{\boldsymbol{\theta}}_i^T]^T$ where $\dot{\boldsymbol{\theta}}_i$ is defined in Eq. (35). The static equations are then developed based on the virtual work principle, which can be expressed as

$$\boldsymbol{\tau}_{ip} = \mathbf{J}_{ip}^T \mathbf{F}_{it}, \quad i = 1, 2, 3 \quad (49)$$

where $\boldsymbol{\tau}_{ip} = [\tau_{ip1} \cdots \tau_{ipn}]^T$ is the $n \times 1$ vector of joint torques of the pseudo-rigid linkage, and $\mathbf{F}_{it} = [\mathbf{f}_{it}^T m_i]^T$ is the 3×1 vector of the tip force (\mathbf{f}_{it}) and tip moment (m_i).

It should be noted that although both τ_{ij} and τ_{ijp} (with $j = 1, \dots, n$), which are obtained from Eqs. (44) and (49) respectively, represent the ij -th pseudo-joint torque, they have different pseudo physical meanings: τ_{ij} is the pseudo-joint torque required to statically resist a wrench applied at the end-effector of the PCR; while τ_{ijp} is the pseudo-joint torque required to statically resist the tip force and moment generated by the tendon tension of the corresponding continuum link.

Equation (49) can be rewritten as

$$\boldsymbol{\tau}_p = \mathbf{J}_p^T \mathbf{F}_t \quad (50)$$

where

$$\boldsymbol{\tau}_p = [\boldsymbol{\tau}_{1p}^T \boldsymbol{\tau}_{2p}^T \boldsymbol{\tau}_{3p}^T]^T, \quad (51)$$

and

$$\mathbf{J}_p = \begin{bmatrix} \mathbf{J}_{1p} & \mathbf{0} & \mathbf{0} \\ \mathbf{0} & \mathbf{J}_{2p} & \mathbf{0} \\ \mathbf{0} & \mathbf{0} & \mathbf{J}_{3p} \end{bmatrix}, \quad (52)$$

which is of dimension $9 \times 3n$ and in which $\mathbf{0}$ is a $3 \times n$ zero matrix, and

$$\mathbf{F}_t = [\mathbf{f}_{1t}^T m_1 \mathbf{f}_{2t}^T m_2 \mathbf{f}_{3t}^T m_3]^T. \quad (53)$$

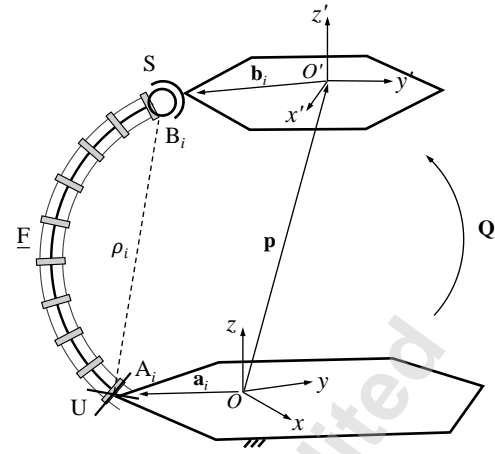


Fig. 6: Kinematic modelling of one leg of the 6-UFS spatial TDPCR.

The vector of tip forces and moments of the three pseudo-rigid linkages of the TDPCR can be obtained as

$$\mathbf{F}_t = \mathbf{J}_p^T \boldsymbol{\tau}_p \quad (54)$$

Similarly to the approach proposed in [16] for motion control of serial tendon-driven continuum robots under PRB assumptions, Eq. (54) can be used to calculate the lengths of the tendons, which in turn are utilised to control the motion of the TDPCR: first, the pseudo-joint coordinates of the TDPCR are readily calculated from the inverse kinematic analysis (as discussed in Section 2.3); second, the relationship given in Eq. (45) is utilised to compute the pseudo-joint torque, τ_{ijp} , leading to

$$\tau_{ijp} = k_{ij} \delta \theta_{ij}, \quad i = 1, 2, 3 \text{ and } j = 1, \dots, n; \quad (55)$$

third, determine the vector of tip forces and moments, \mathbf{F}_t , by substituting Eq. (55) into Eq. (54); finally, the lengths of the tendons required to drive the continuum links are calculated by the manipulator specific model developed in [16] based on the obtained \mathbf{F}_t .

4 Kinematic Modelling of Spatial and Kinematically Redundant TDPCRs

The approach for kinematic modelling outlined in the preceding sections can also be applied to spatial and redundant TDPCRs as we will demonstrate by two case studies of a spatial 6-DOF and a planar kinematically redundant hybrid $(3+3)$ -DOF TDPCRs.

4.1 A Spatial 6-UFS TDPCR

One leg of the 6-UFS spatial TDPCR which is a variant of the conventional Gough-Stewart platform is schematically illustrated in Fig. 6. The moving platform of the TDPCR is

connected to the base by 6 identical UFS legs, where U and S respectively denote a passive universal joint and a passive spherical joint. Even if a Cartesian wrench is applied to the moving platform, an out-of-plane motion of the continuum links will not be generated. This is because each continuum link of the TDPCR can only resist forces passing through the passive spherical and universal joints in the same link, and the force is located on the bending plane of this link at any instant.

Constraint equations on the squared length between points A_i and B_i (with $i = 1, \dots, 6$) for each leg are established in a manner similar to those shown in Eq. (1). Velocity (under both CC and PRB assumptions) and static equations can then be straightforwardly developed by taking the time derivative of the six constraint equations, as briefly addressed below.

The vector of Cartesian velocities is defined as $\mathbf{t} = [\mathbf{p}^T \ \boldsymbol{\omega}^T]^T$, where \mathbf{p} and $\boldsymbol{\omega} \in \mathbb{R}^3$ are respectively the Cartesian linear and angular velocities of the moving platform. Upon differentiation with respect to time of the constraint equations, one obtains

$$\rho \dot{\mathbf{p}} = \mathbf{r}_i^T \dot{\mathbf{p}} + (\mathbf{Q} \mathbf{b}_{i0} \times \mathbf{r}_i)^T \boldsymbol{\omega}, \quad i = 1, 2, 3. \quad (56)$$

where

$$\mathbf{r}_i = \mathbf{p} + \mathbf{Q} \mathbf{b}_{i0} - \mathbf{a}_i, \quad i = 1, \dots, 6, \quad (57)$$

in which $\mathbf{Q} \in SO(3)$ is the rotation matrix of the moving frame with respect to the base frame, and \mathbf{b}_{i0} stands for vector \mathbf{b}_i when expressed in the moving frame. The velocity equations are written in the form similar to Eq. (17). Jacobian \mathbf{J} is written as

$$\mathbf{J} = \begin{bmatrix} \mathbf{r}_1^T (\mathbf{Q} \mathbf{b}_{10} \times \mathbf{r}_1)^T \\ \vdots \\ \mathbf{r}_6^T (\mathbf{Q} \mathbf{b}_{60} \times \mathbf{r}_6)^T \end{bmatrix}. \quad (58)$$

Matrix \mathbf{J} is of dimension 6×6 , in which each row represents a Plücker line passing through points A_i and B_i in the i th leg.

Under the CC assumption, variables of the time derivative of the six tendons (only one of the two tendons of a continuum link is considered) are given as $\dot{\ell} = [\dot{\ell}_{11} \ \dots \ \dot{\ell}_{61}]^T$, and Jacobian \mathbf{K} is expressed as

$$\mathbf{K} = \text{diag} [k_1, \dots, k_6], \quad (59)$$

where $k_i, i = 1, \dots, 6$ can be calculated using Eq. (20).

While under the PRB assumption, and referring to Fig. 5, Eq. (34) can be reformulated for the 6-UFS TDPCR

$$\rho_i \dot{\mathbf{p}}_i = \mathbf{r}_i^T [\mathbf{e}_i \times \mathbf{r}_{i3} \ \dots \ \mathbf{e}_i \times \mathbf{r}_{in}] \begin{bmatrix} \dot{\theta}_{i3} \\ \vdots \\ \dot{\theta}_{in} \end{bmatrix}, \quad i = 1, \dots, 6 \quad (60)$$

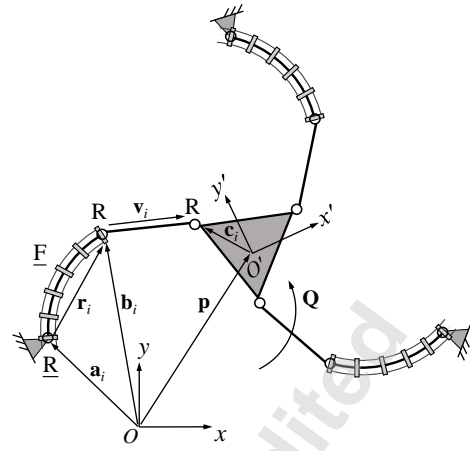


Fig. 7: Kinematic modelling of a planar (3+3)-DOF kinematically redundant hybrid 3-RFRR TDPCR.

where \mathbf{e}_i is the unit direction vector of the pseudo-rigid joints in the i th continuum link. Note that in this case \mathbf{r}_i and $\mathbf{r}_{ij}, j = 3, \dots, n \in \mathbb{R}^3$, and the first two joint variables associate with the universal joint in each leg vanish since \mathbf{r}_i coincides with \mathbf{r}_{i1} and \mathbf{r}_{i2} . Jacobian \mathbf{K}_θ can then be expressed as

$$\mathbf{K}_\theta = \begin{bmatrix} \mathbf{k}_{1\theta} & & \\ & \ddots & \\ & & \mathbf{k}_{6\theta} \end{bmatrix} \quad (61)$$

in which

$$\mathbf{k}_{i\theta} = \mathbf{r}_i^T [\mathbf{e}_i \times \mathbf{r}_{i3} \ \dots \ \mathbf{e}_i \times \mathbf{r}_{in}], \quad i = 1, \dots, 6. \quad (62)$$

And the vector of joint velocities is written as $\dot{\boldsymbol{\theta}} = [\dot{\boldsymbol{\theta}}_1^T \ \dots \ \dot{\boldsymbol{\theta}}_6^T]^T$ with $\dot{\boldsymbol{\theta}}_i = [\dot{\theta}_{i3} \ \dots \ \dot{\theta}_{in}]^T, i = 1, \dots, 6$.

Given Jacobian matrices \mathbf{J} and \mathbf{K}_θ , we can develop the static equations of the 6-UFS TDPCR by the procedure which is demonstrated in Section 3.1.

The static equations of the six continuum links (pseudo-rigid linkages) in the absence of external loading consists of the static equation of each of these links and is written in a form similar to Eq. (50), and the velocity Jacobian of each pseudo-rigid linkage is defined in Eq. (48). It is not necessary to express the vector entries in \mathbb{R}^3 when developing the velocity Jacobian. This is because the continuum link of the 6-UFS TDPCR can only produce an in-plane bending, although the bending plane varies with the rotation of the universal joint connected to the link, it is easily determined since the joint variables of the universal joint can be solved from the inverse kinematic analysis of the TDPCR.

4.2 A Planar 3-RFRR Kinematically Redundant Hybrid TDPCR

Consider the planar 3-RFRR (3+3)-DOF kinematically redundant hybrid TDPCR (see Fig. 7), which consists in re-

placing the second actuated revolute joint and adjacent links in each of the legs of the rigid planar 3-RRRR (3 + 3)-DOF kinematically redundant hybrid parallel robot counterpart [35] by an actuated continuum link. Constraint equations on the constant squared length of each of the passive RR redundant links can be established, which are written in the same form as that shown in Eq. (21). The velocity (under both CC and PRB assumptions) and static equations are then readily developed based on the time derivative of the constraint equations. However, it should be noted that different from the expression of vector \mathbf{r}_i under CC assumption given in Eq. (24), in this case vector \mathbf{r}_i is written as

$$\mathbf{r}_i = \rho_i \begin{bmatrix} \cos \theta_{i1} \\ \sin \theta_{i1} \end{bmatrix}, \quad i = 1, 2, 3 \quad (63)$$

where θ_{i1} is the coordinate of the actuated revolute joint in the i -th leg. Differentiating \mathbf{r}_i with respect to time leads to

$$\dot{\mathbf{r}}_i = \begin{bmatrix} -\rho_i \sin \theta_{i1} & \cos \theta_{i1} \\ \rho_i \cos \theta_{i1} & \sin \theta_{i1} \end{bmatrix} \begin{bmatrix} \dot{\theta}_{i1} \\ \dot{\rho}_i \end{bmatrix}. \quad (64)$$

Substituting Eqs. (14) and (8) into Eq. (64), then, Eq. (64) can be rewritten as

$$\dot{\mathbf{r}}_i = \mathbf{M}_i \begin{bmatrix} \dot{\theta}_{i1} \\ \dot{\ell}_{i1} \end{bmatrix} \quad (65)$$

with

$$\mathbf{M}_i = \begin{bmatrix} -\rho_i \sin \theta_{i1} & \alpha_i \lambda_i \cos \theta_{i1} \\ \rho_i \cos \theta_{i1} & \alpha_i \lambda_i \sin \theta_{i1} \end{bmatrix}, \quad i = 1, 2, 3. \quad (66)$$

Therefore, Jacobian \mathbf{K} has the following form:

$$\mathbf{K} = \begin{bmatrix} \mathbf{v}_1^T \mathbf{M}_1 & \mathbf{0} & \mathbf{0} \\ \mathbf{0} & \mathbf{v}_2^T \mathbf{M}_2 & \mathbf{0} \\ \mathbf{0} & \mathbf{0} & \mathbf{v}_3^T \mathbf{M}_3 \end{bmatrix} \quad (67)$$

in which $\mathbf{0}$ is the 1×2 zero vector. The dimension of matrix \mathbf{K} is 3×6 , and the redundancy of the 3-RFRR TDPCR is apparent from matrix \mathbf{K} , which contains two columns for the two actuated joints (\mathbf{R} and \mathbf{F}) in each of the legs.

It was shown in this and preceding sections that, under CC and PRB assumptions, kinematic and static modelling, and formulations for solving the differential inverse kinematic and forward kinematic problems, of TDPCRs can be accomplished using the approaches that are widely implemented in the modelling of rigid parallel robots. These approaches are demonstrated by several case studies and are readily applied to other TDPCRs. In the following section, we will show the consistency of singularity analysis of TDPCRs and rigid parallel robots. Moreover, an example study is provide to illustrate the singular configurations and to validate the kinematic models.

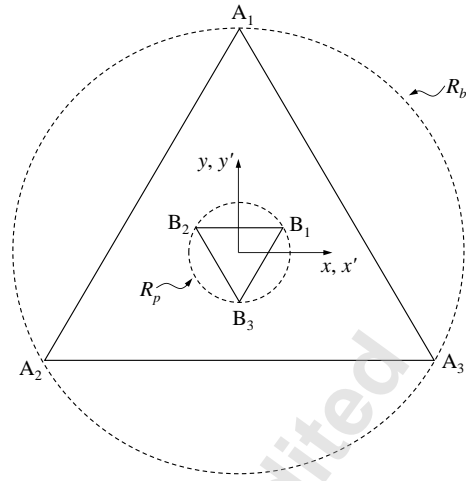


Fig. 8: Initial configuration of the planar 3-RFR TDPCR.

5 Singularity Analysis of TDPCRs

Similar to rigid parallel robots, TDPCRs also suffer from the so-called type I and type II singularities [36]. A type II singularity occurs when Jacobian matrix \mathbf{J} (which consists of the Plücker lines) becomes singular. It can be observed that this kind of Jacobian matrix of a TDPCR is identical to that of its rigid counterpart. Therefore, type II singularities can be detected using established techniques, e.g., Grassmann line geometry, which are widely implemented in singularity analysis of rigid parallel robots. For example, the planar 3-RFR TDPCR is in a type II singular configuration when the three Plücker lines intersect at a common point or when they are parallel to each other. Such kind of singularities mainly exist within the workspace and can reduce the rotational capability of the TDPCR significantly.

Type I singularity conditions of the TDPCRs under PRB assumption are similar to those of the corresponding kinematically redundant parallel robots (see, for instance [35]), which is easily detected and the detailed analysis is not shown here. For PCRs under CC assumption, a type I singularity occurs when the curvature, κ_i , of the i -th continuum link is equal to 0 or reaches the extreme value. In the former case, for example, the diagonal elements in Jacobian matrix \mathbf{K} , which are defined in Eqs. (20) and (30) for the planar 3-RFR and 3-FRR TDPCRs respectively, are undefined because κ_i appears in the denominators, in which case the i -th continuum link is fully extended. While in the latter case, the i -th continuum link is fully folded, i.e., the start and end points of the link coincide with each other. Nevertheless, the latter case can be easily avoided in practice by mechanical limits. Type I singularities of the TDPCRs under CC assumption also occur when any of the diagonal elements in Jacobian matrix \mathbf{K} is equal to 0.

Singularity analysis of another type of PCRs based on the kinemastatic model is provided in [37]. It is shown that type I singularities correspond to the workspace boundary, and type II singularities occur when the potential energy of the robot has a local isovalue. Although the singularity conditions of the TDPCRs obtained here are similar to those

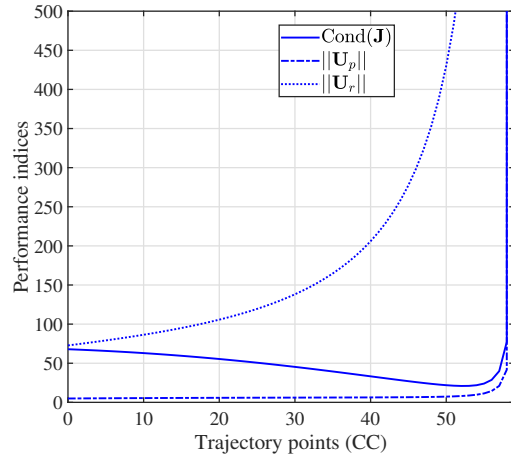


Fig. 9: Performance indices of the 3-RFR TDPCR under CC assumption.

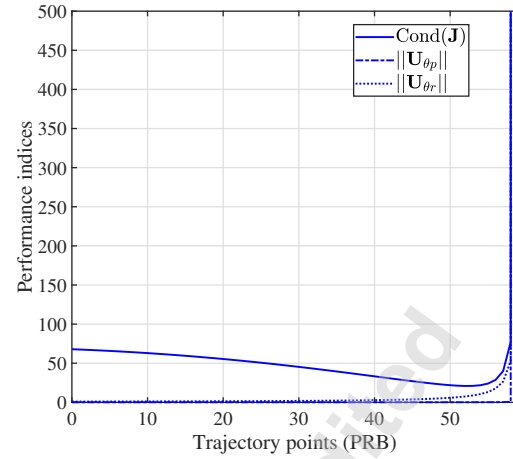


Fig. 11: Performance indices of the 3-RFR TDPCR under PRB assumption.

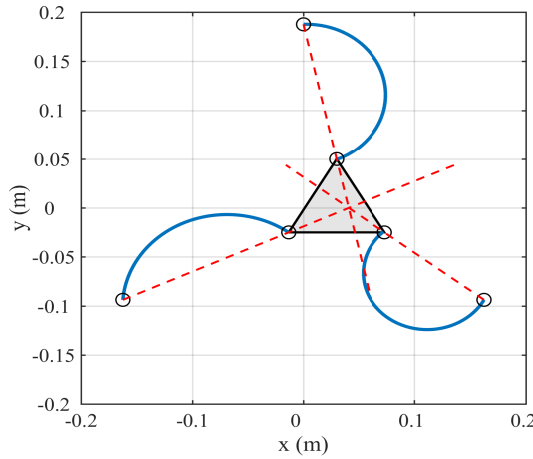


Fig. 10: A singular configuration of the 3-RFR TDPCR under CC assumption. Revolute joints and Plücker lines are respectively represented by circles and red dashed line segments. For simplicity, only the backbone of each of the continuum links is shown.

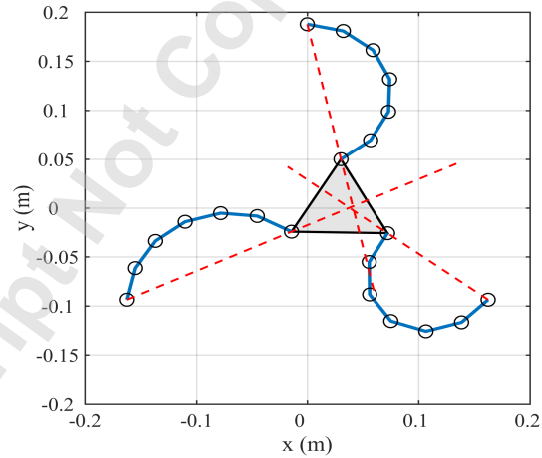


Fig. 12: A singular configuration of the 3-RFR TDPCR under PRB assumption. Revolute joints (including the pseudo ones) and Plücker lines are respectively represented by circles and red dashed line segments.

shown in [37], a different strategy is utilised. This is because, different from the passive continuum links of the architectures in [37], the continuum segments of the TDPCRs studied in this paper are actuated, thereby it is more convenient to perform singularity analysis using a geometric method.

5.1 Example

We provide a case study based on the planar 3-RFR TDPCR (see Fig. 2) to validate the kinematic models developed using both the CC and PRB assumptions. We will show that the performance indices, e.g., condition number and kinematic sensitivities [38], which are used to detect the closeness to a singular configuration of rigid parallel robots, can also be used for the determination of singularities of TDPCRs.

The base and moving platform of the 3-RFR TDPCR are modelled as equilateral triangles (see Fig. 8). The geometric parameters are given as

$$R_b = 0.19 \text{ m}, R_p = 0.05 \text{ m}, d = 0.005 \text{ m} \\ \ell_i = 0.2 \text{ m}, i = 1, 2, 3$$

where R_b and R_p are respectively the circumradii of the base and moving platform. The geometry of the base is given as

$$\mathbf{a}_1 = R_b \begin{bmatrix} 0 \\ 1 \end{bmatrix} \\ \mathbf{a}_2 = R_b \begin{bmatrix} -\cos(\pi/6) \\ -\sin(\pi/6) \end{bmatrix} \\ \mathbf{a}_3 = R_b \begin{bmatrix} \cos(\pi/6) \\ -\sin(\pi/6) \end{bmatrix},$$

while the geometry of the moving platform is given as

$$\begin{aligned} \mathbf{b}_1 &= R_p \begin{bmatrix} \cos(\pi/6) \\ \sin(\pi/6) \end{bmatrix} \\ \mathbf{b}_2 &= R_p \begin{bmatrix} -\cos(\pi/6) \\ \sin(\pi/6) \end{bmatrix} \\ \mathbf{b}_3 &= -R_p \begin{bmatrix} 0 \\ 1 \end{bmatrix}. \end{aligned}$$

A trajectory which consists of a translation accompanied by a rotation is performed. The trajectory is divided into 60 discrete configurations where the position and orientation of the moving platform in this trajectory are given as

$$\mathbf{p} = \begin{bmatrix} x \\ 0 \end{bmatrix} \quad (68)$$

$$\mathbf{Q} = \begin{bmatrix} \cos(\frac{1}{3}\eta\pi) & -\sin(\frac{1}{3}\eta\pi) \\ \sin(\frac{1}{3}\eta\pi) & \cos(\frac{1}{3}\eta\pi) \end{bmatrix}, \quad (69)$$

with

$$0 \text{ m} \leq x \leq 0.03 \text{ m}, \quad 0 \leq \eta \leq 1. \quad (70)$$

Three performance indices including the condition number of Jacobian \mathbf{J} (in spite of the physical meaning of its numerical value), the 2-norm of the position part of matrices \mathbf{U} (defined in Eq. (39)) and \mathbf{U}_θ (defined in Eq. (40)), noted $\|\mathbf{U}_p\|$ and $\|\mathbf{U}_{\theta p}\|$, and the 2-norm of the rotation part of these matrices, noted $\|\mathbf{U}_r\|$ and $\|\mathbf{U}_{\theta r}\|$, are evaluated throughout the trajectory. The indices other than the condition number correspond to the kinematic sensitivities. The evolution of these indices for the 3-RFR TDPCR under CC assumption is shown in Fig. 9, where the numerical values clearly indicate that the TDPCR is approaching a singular configuration because they increase to infinity. The last pose of the TDPCR in this trajectory is illustrated in Fig. 10. It can be observed that the TDPCR is in a type II singular configuration since the three Plücker lines (represented by red dashed line segments) intersect at a common point.

In this simulation, the number of pseudo-rigid links in each of the legs of the TDPCR under PRB assumption is selected to be $n = 6$. Under the PRB assumption, the investigation of the performance indices of the TDPCR is identical to that of the corresponding kinematically redundant rigid parallel robot. The joint values throughout the trajectory are equal to the minimum norm term of the general solution, i.e., the null space term is neglected. The evolution of the indices throughout the trajectory is shown in Fig. 11. It can be observed, which is similar to that with CC assumption, that the numerical values increase to infinity when the TDPCR approaches a singular configuration (see Fig. 12). It can also be observed that the numerical values of $\|\mathbf{U}_{\theta r}\|$ are smaller and more stable than those of $\|\mathbf{U}_r\|$ until the TDPCR reaches the singularity, which may lead to a conclusion that the rotation of the TDPCR under CC assumption is more sensitive to be affected by singularities.

The numerical values of the performance indices clearly indicate the singularities, which is consistent with the results obtained with Grassmann line geometry, provided that the kinematic models accurately represent the configurations of the TDPCR.

6 Conclusion

In this paper, velocity and static equations, forward and differential inverse kinematic solutions, and singularity conditions of TDPCRs are proposed. It is shown that constraint equations which are similar to those of the rigid parallel robots can be established, which are essential for developing the velocity equations. A static model of the whole robot under PRB assumption is obtained. However, it has been indicated that the Jacobian matrices appropriately represent the configuration of the TDPCR only if the magnitude of the Cartesian wrench is limited. A static model of each of the continuum links of a TDPCR is also provided which can be further implemented in the motion control of the robot. Type II singular conditions of TDPCRs are identical to those of their rigid counterparts, namely singularities are governed by the orientation of the Plücker lines in the Jacobian matrix, which are demonstrated by detecting the numerical values of three performance indices.

It should be noted that in this paper the common techniques used for kinematic and static analysis of rigid parallel robots are applied only to a specific type of PCRs, i.e., TDPCRs. The possibility of applying these techniques to other types of PCRs needs further research. Moreover, an approach, such as the principle of minimization of potential energy, could be used to detect when the CC assumption is invalid under external loading so that the PRB assumption should be exploited. The feasibility of such an approach needs to be investigated in the future. Current and future work also includes dynamic analysis of the proposed architectures, experimental validation of the accuracy of the kinematic and static models for control purpose, and kinematic and dynamic analysis of TDPCRs with more than two tendons and with multi segments in each of the continuum links.

TDPCRs are subjected to constraint conditions similar to those of rigid parallel robots, making it possible to unify the modelling approaches for such type of robots with those for the latter ones. One of the benefits of this paradigm is that it can facilitate the synthesis, design, and modelling of novel architectures of TDPCRs.

Acknowledgements

The authors would like to thank Sven Lilge, PhD candidate at the Continuum Robotics Laboratory (University of Toronto) for reading the manuscript and providing useful comments on the constant curvature and pseudo-rigid-body assumptions.

References

- [1] Burgner-Kahrs, J., Rucker, D. C., and Choset, H., 2015. "Continuum robots for medical applications: A survey". *IEEE Transactions on Robotics*, **31**(6), pp. 1261–1280.
- [2] Goldman, R. E., Bajo, A., MacLachlan, L. S., Pickens, R., Herrell, S. D., and Simaan, N., 2012. "Design and performance evaluation of a minimally invasive telerobotic platform for transurethral surveillance and intervention". *IEEE Transactions on Biomedical Engineering*, **60**(4), pp. 918–925.
- [3] Burgner, J., Rucker, D. C., Gilbert, H. B., Swaney, P. J., Russell, P. T., Weaver, K. D., and Webster, R. J., 2013. "A telerobotic system for transnasal surgery". *IEEE/ASME Transactions on Mechatronics*, **19**(3), pp. 996–1006.
- [4] Dong, X., Axinte, D., Palmer, D., Cobos, S., Raffles, M., Rabani, A., and Kell, J., 2017. "Development of a slender continuum robotic system for on-wing inspection/repair of gas turbine engines". *Robotics and Computer-Integrated Manufacturing*, **44**, pp. 218–229.
- [5] Santiago, J. L. C., Walker, I. D., and Godage, I. S., 2015. "Continuum robots for space applications based on layer-jamming scales with stiffening capability". In 2015 IEEE Aerospace Conference, IEEE, pp. 1–13.
- [6] Chirikjian, G. S., and Burdick, J. W., 1994. "A modal approach to hyper-redundant manipulator kinematics". *IEEE Transactions on Robotics and Automation*, **10**(3), pp. 343–354.
- [7] Jones, B. A., and Walker, I. D., 2006. "Kinematics for multisection continuum robots". *IEEE Transactions on Robotics*, **22**(1), pp. 43–55.
- [8] Webster III, R. J., and Jones, B. A., 2010. "Design and kinematic modeling of constant curvature continuum robots: A review". *The International Journal of Robotics Research*, **29**(13), pp. 1661–1683.
- [9] Dupont, P. E., Lock, J., Itkowitz, B., and Butler, E., 2009. "Design and control of concentric-tube robots". *IEEE Transactions on Robotics*, **26**(2), pp. 209–225.
- [10] Rucker, D. C., and Webster III, R. J., 2011. "Statics and dynamics of continuum robots with general tendon routing and external loading". *IEEE Transactions on Robotics*, **27**(6), pp. 1033–1044.
- [11] Mahvash, M., and Dupont, P. E., 2011. "Stiffness control of surgical continuum manipulators". *IEEE Transactions on Robotics*, **27**(2), pp. 334–345.
- [12] Tang, W., Wan, T. R., Gould, D. A., How, T., and John, N. W., 2012. "A stable and real-time nonlinear elastic approach to simulating guidewire and catheter insertions based on Cosserat rod". *IEEE Transactions on Biomedical Engineering*, **59**(8), pp. 2211–2218.
- [13] Howell, L. L., 2001. *Compliant Mechanisms*. John Wiley & Sons, Inc., New York.
- [14] Su, H.-J., 2009. "A pseudorigid-body 3R model for determining large deflection of cantilever beams subject to tip loads". *ASME Journal of Mechanisms and Robotics*, **1**(2), p. 021008.
- [15] Khoshnam, M., Khalaji, I., and Patel, R. V., 2015. "A robotics-assisted catheter manipulation system for cardiac ablation with real-time force estimation". In 2015 IEEE/RSJ International Conference on Intelligent Robots and Systems (IROS), IEEE, pp. 3202–3207.
- [16] Roesthuis, R. J., and Misra, S., 2016. "Steering of multisegment continuum manipulators using rigid-link modeling and FBG-based shape sensing". *IEEE Transactions on Robotics*, **32**(2), pp. 372–382.
- [17] Huang, S., Meng, D., Wang, X., Liang, B., and Lu, W., 2019. "A 3D static modeling method and experimental verification of continuum robots based on pseudo-rigid body theory". In 2019 IEEE/RSJ International Conference on Intelligent Robots and Systems (IROS), IEEE, pp. 4672–4677.
- [18] Rao, P., Peyron, Q., Lilge, S., and Burgner-Kahrs, J., 2021. "How to model tendon-driven continuum robots and benchmark modelling performance". *Frontiers in Robotics and AI*, **7**, p. 223.
- [19] Till, J., Bryson, C. E., Chung, S., Orekhov, A., and Rucker, D. C., 2015. "Efficient computation of multiple coupled Cosserat rod models for real-time simulation and control of parallel continuum manipulators". In 2015 IEEE International Conference on Robotics and Automation (ICRA), IEEE, pp. 5067–5074.
- [20] Hopkins, J. B., Rivera, J., Kim, C., and Krishnan, G., 2015. "Synthesis and analysis of soft parallel robots comprised of active constraints". *ASME Journal of Mechanisms and Robotics*, **7**(1), p. 011002.
- [21] Singh, I., Singh, M., Pathak, P. M., and Merzouki, R., 2017. "Optimal work space of parallel continuum manipulator consisting of compact bionic handling arms". In 2017 IEEE International Conference on Robotics and Biomimetics (ROBIO), IEEE, pp. 258–263.
- [22] Altuzarra, O., Caballero, D., Zhang, Q., and Campa, F. J., 2018. "Kinematic characteristics of parallel continuum mechanisms". In International Symposium on Advances in Robot Kinematics, Springer, pp. 293–301.
- [23] White, E. L., Case, J. C., and Kramer-Bottiglio, R., 2018. "A soft parallel kinematic mechanism". *Soft robotics*, **5**(1), pp. 36–53.
- [24] Yang, Z., Zhu, X., and Xu, K., 2018. "Continuum delta robot: a novel translational parallel robot with continuum joints". In 2018 IEEE/ASME International Conference on Advanced Intelligent Mechatronics (AIM), IEEE, pp. 748–755.
- [25] Young, E. M., and Kuchenbecker, K. J., 2019. "Implementation of a 6-DOF parallel continuum manipulator for delivering fingertip tactile cues". *IEEE Transactions on Haptics*, **12**(3), pp. 295–306.
- [26] Mauzé, B., Dahmouche, R., Laurent, G. J., André, A. N., Rougeot, P., Sandoz, P., and Clévy, C., 2020. "Nanometer precision with a planar parallel continuum robot". *IEEE Robotics and Automation Letters*, **5**(3), pp. 3806–3813.
- [27] Nuelle, K., Sternecker, T., Lilge, S., Xiong, D., Burgner-Kahrs, J., and Ortmaier, T., 2020. "Modeling, calibration, and evaluation of a tendon-actuated planar parallel continuum robot". *IEEE Robotics and Automation Letters*

- ters, **5**(4), pp. 5811–5818.
- [28] Lilge, S., Nuelle, K., Boettcher, G., Spindeldreier, S., and Burgner-Kahrs, J., 2021. “Tendon actuated continuous structures in planar parallel robots: A kinematic analysis”. *ASME Journal of Mechanisms and Robotics*, **13**(1), p. 011025.
 - [29] Böttcher, G., Lilge, S., and Burgner-Kahrs, J., 2021. “Design of a reconfigurable parallel continuum robot with tendon-actuated kinematic chains”. *IEEE Robotics and Automation Letters*, **6**(2), pp. 1272–1279.
 - [30] Gosselin, C., and Schreiber, L.-T., 2016. “Kinematically redundant spatial parallel mechanisms for singularity avoidance and large orientational workspace”. *IEEE Transactions on Robotics*, **32**(2), pp. 286–300.
 - [31] Merlet, J.-P., 2004. “Solving the forward kinematics of a Gough-type parallel manipulator with interval analysis”. *The International Journal of robotics research*, **23**(3), pp. 221–235.
 - [32] Kong, X., 2008. “Forward kinematics and singularity analysis of a 3-RPR planar parallel manipulator”. In *Advances in Robot Kinematics: Analysis and Design*. Springer, pp. 29–38.
 - [33] Wen, K., and Gosselin, C. M., 2020. “Forward kinematic analysis of kinematically redundant hybrid parallel robots”. *ASME Journal of Mechanisms and Robotics*, **12**(6), p. 061008.
 - [34] Gosselin, C. M., Sefrioui, J., and Richard, M. J., 1992. “Solutions polynomiales au problème de la cinématique directe des manipulateurs parallèles plans à trois degrés de liberté”. *Mechanism and Machine Theory*, **27**(2), pp. 107–119.
 - [35] Wen, K., and Gosselin, C., 2019. “Kinematically redundant hybrid robots with simple singularity conditions and analytical inverse kinematic solutions”. *IEEE Robotics and Automation Letters*, **4**(4), pp. 3828–3835.
 - [36] Gosselin, C., Angeles, J., et al., 1990. “Singularity analysis of closed-loop kinematic chains”. *IEEE transactions on robotics and automation*, **6**(3), pp. 281–290.
 - [37] Briot, S., and Goldsztejn, A., 2021. “Singularity conditions for continuum parallel robots”. *IEEE Transactions on Robotics*.
 - [38] Cardou, P., Bouchard, S., and Gosselin, C., 2010. “Kinematic-sensitivity indices for dimensionally non-homogeneous jacobian matrices”. *IEEE Transactions on Robotics*, **26**(1), pp. 166–173.